

New Methods toward Minimizing the Slow Speed Bias Associated with Atmospheric Motion Vectors

WAYNE C. BRESKY

I.M. Systems Group, Rockville, Maryland

JAIME M. DANIELS

NOAA/NESDIS Office of Research and Applications, Camp Springs, Maryland

ANDREW A. BAILEY

I.M. Systems Group, Rockville, Maryland

STEVEN T. WANZONG

Cooperative Institute for Meteorological Satellite Studies, University of Wisconsin—Madison, Madison, Wisconsin

(Manuscript received 15 November 2011, in final form 22 June 2012)

ABSTRACT

Comparisons between satellite-derived winds and collocated rawinsonde observations often show a pronounced slow speed bias at mid- and upper levels of the atmosphere. A leading cause of the slow speed bias is the improper assignment of the tracer to a height that is too high in the atmosphere. Height errors alone cannot fully explain the slow bias, however. Another factor influencing the speed bias is the size of the target window used in the tracking step. Tracking with a large target window can cause excessive averaging to occur and a smoothing of the instantaneous wind field. Conversely, if too small a window is specified, there is an increased risk of finding a false match. The authors have developed a new “nested tracking” approach that isolates the dominant local motion within a cloud scene and minimizes the smoothing of the motion estimate. A major advantage of the new approach is the ability to identify which pixels within the cloud scene are contributing to the tracking solution. Knowing which pixels contribute to the dominant motion allows for a more representative height to be derived, thereby directly linking the height assignment to the tracking process, which is an important goal for producers of global atmospheric motion vector (AMV) data. When compared with equivalent rawinsondes, the AMVs derived with the new approach show a considerable improvement in the speed bias and root-mean-square error over a control set of AMVs derived with more-conventional methods.

1. Introduction

Cloud-tracked winds produced from satellite-image sequences have long exhibited a pronounced slow speed bias at mid- (400–700 hPa) and upper (100–400 hPa) levels of the atmosphere when compared with rawinsonde profiles and other wind measurements (e.g., Schmetz et al. 1993, their Fig. 4; Bormann et al. 2002; von Bremen et al. 2008; Rohn et al. 2001). Monitoring statistics from the Met

Office that compare atmospheric motion vectors (AMV) from several global AMV data producers with the Met Office model background field reveal that the slow speed bias is particularly pronounced during the extratropical winter season (Forsythe and Saunders 2008). At the National Oceanic and Atmospheric Administration National Environmental Satellite, Data, and Information Service (NOAA/NESDIS), routine verification of operational cloud-track winds against rawinsonde observations also reveals a slow speed bias under similar conditions. This is illustrated in Fig. 1, which shows a time series plot of mean vector difference (MVD) and speed bias statistics between *Geostationary Operational*

Corresponding author address: Wayne Bresky, I.M. Systems Group, Inc., 3206 Tower Oaks Blvd., Suite 300, Rockville, MD 20852.
E-mail: wayne.bresky@noaa.gov

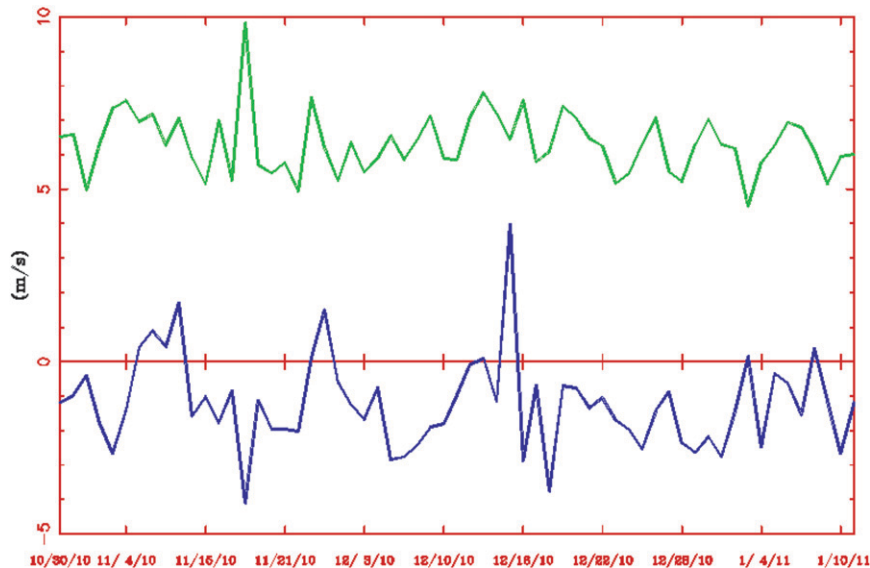


FIG. 1. MVD (green) and speed bias (blue; satellite – rawinsonde) for *GOES-12* upper-level (100–400 hPa) IR cloud-drift winds for the period from 30 Oct 2010 to 10 Jan 2011.

Environmental Satellite-12 (GOES-12) upper-level cloud-track winds and rawinsondes during the Northern Hemisphere winter season. Note the consistent $1\text{--}2\text{ m s}^{-1}$ slow speed bias throughout the time period. This figure is even more remarkable when one considers that the height assignments of these winds have been adjusted to better fit a combined forecast and satellite wind data analysis, as well as having had a speed bias correction applied in certain situations (Hayden and Nieman 1996; Velden et al. 1998). Without this postprocessing, the slow speed bias would be even more pronounced than what is shown by this figure. The impact of the postprocessing performed at NOAA/NESDIS on the speed bias has been discussed by several authors (Nieman et al. 1997; von Bremen et al. 2008; Forsythe and Saunders 2008).

A leading contributor to the observed slow speed bias is a poorly assigned height (Bormann et al. 2002). In general, a tracer that is assigned to be too high in the atmosphere will exhibit a slow speed bias and one assigned to be too low in the atmosphere will exhibit a fast speed bias. Height-assignment errors can produce a slow speed bias, but recent work has shown that they do not fully explain the bias (von Bremen et al. 2008). A second explanation is that some cloud scenes may not behave as passive tracers or may be dominated by evolving, rather than translating, features (e.g., stationary wave clouds and developing thunderstorms). Other factors that must be considered are that the cloud scene being tracked often contains motions from different levels of the atmosphere (Velden and Bedka 2009) or may contain motions of varying length and time scales. For example,

the motion of a frontal system is usually very different from the local motion within the frontal zone itself. In this scenario, the retrieved motion from conventional tracking approaches is often a spatial average of these two motions.

To facilitate the discussion that follows, we have included a schematic (Fig. 2) that shows the basic concepts associated with the feature-tracking algorithm used operationally at NOAA/NESDIS. The first step in the algorithm is to build an image loop from three consecutive image times. Next, the middle image is divided into small subregions called “target scenes” and each target scene is processed to determine whether it contains a suitable tracer. If the target passes quality checks [see Nieman et al. (1997) for details], an initial height is assigned to the feature using a cold sample (coldest 25%) of pixels contained within the scene. After the target is assigned a height, a forecast wind, valid at the center of the target box and at the assigned height, is utilized to position a search region—typically much larger in size than the target scene—in the subsequent image. Last, the search region is examined to find the cloud scene that most closely resembles the initial target (a linear correlation measure is computed in the NESDIS algorithm) and a displacement is computed.

Recent work by Sohn and Borde (2008, hereinafter referred to as SB) and Cho et al. (2008, hereinafter referred to as CHO) has shown a direct link between the size of the target window and the magnitude of the slow speed bias. To be specific, they noted that as the target-window size is reduced the average speed of the derived

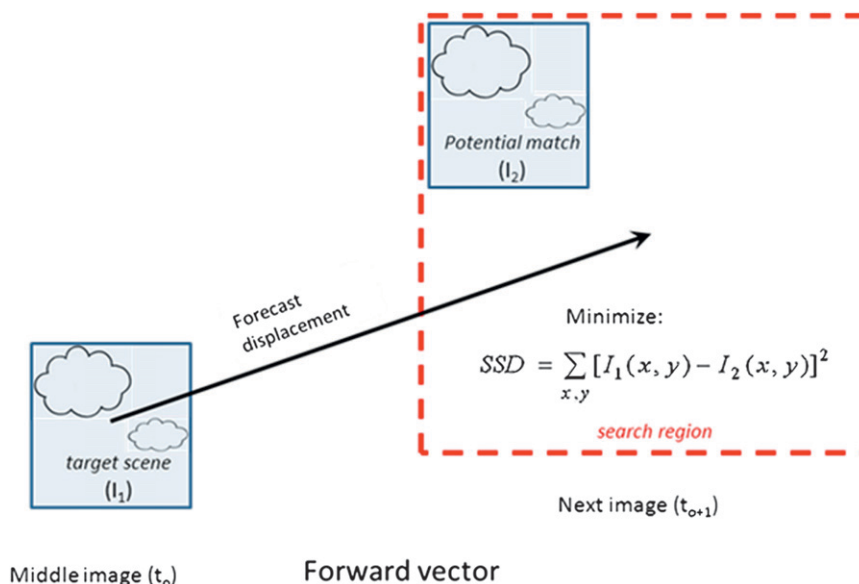


FIG. 2. Schematic that shows the basic concepts associated with the feature-tracking algorithm used at NOAA/NESDIS. Targets are selected from the middle image of a three-image loop and are tracked forward and backward in time. The two displacements are averaged to produce a final motion estimate. Only the forward vector is shown in the figure.

wind increases. Furthermore, SB and CHO also observed that the smaller window size decreases the average height of the winds. It is clear that both of these factors will produce a smaller slow speed bias. Using a small target window also increases the risk of finding false matches, however. As a consequence, the overall impact on the quality of the derived winds is a reduction in the speed bias that comes at the expense of higher RMS errors. One tempting approach to this challenge is simply to reduce the time interval between tracking images. As shown in the next section, however, this should not be done without first considering the spatial resolution of the imagery being used. Although a shorter time interval might be effective at reducing correlation errors, it also implies smaller displacements, which, in turn, imply that errors arising from subpixel displacements take on greater relative importance. Most operational wind producers employ some type of interpolation to avoid the speed “binning” that would otherwise occur from processing satellite data with discrete pixel resolutions of a few kilometers. The operational NOAA/NESDIS algorithm uses the sum of squared differences (SSD) values surrounding the minimum in the linear interpolation to refine the integer displacement.

Complicating matters further is the observation of Borde and Oyama (2008) that the pixels having the greatest influence on the tracking solution are not necessarily the same pixels used to assign a height to the

tracer. Most producers of satellite-derived winds use the coldest pixels from the target scene (Genkova et al. 2008) to assign height without regard to their level of importance in the tracking process. The implied disconnect between the two processing steps can lead to poor-quality winds and large verification errors.

In this paper, we extend the results of earlier testing by SB and CHO by studying the impact of varying image-loop intervals, as well as varying target-window sizes, on the quality of the derived AMVs. Note that the smallest target-window size studied in this paper, 5×5 pixels, is smaller than the smallest window tested by SB and CHO. The reason for testing such a small window will become obvious in later sections.

The rest of the paper is organized as follows: Section 2 summarizes the testing performed with varying image time intervals and target-box sizes and includes a discussion of the new findings as they relate to the earlier results of SB and CHO. In section 3, we introduce a new tracking method that we refer to as “nested tracking.” The new method minimizes the spatial smoothing associated with using a large target window and at the same time avoids the risk of finding a false match. Another new method is introduced that exploits the output from nested tracking to assign a more representative height to the tracer. In section 4, we discuss the impacts on quality of the new nested-tracking and target-height-assignment approaches. In section 5 we summarize our findings and discuss areas of future research.

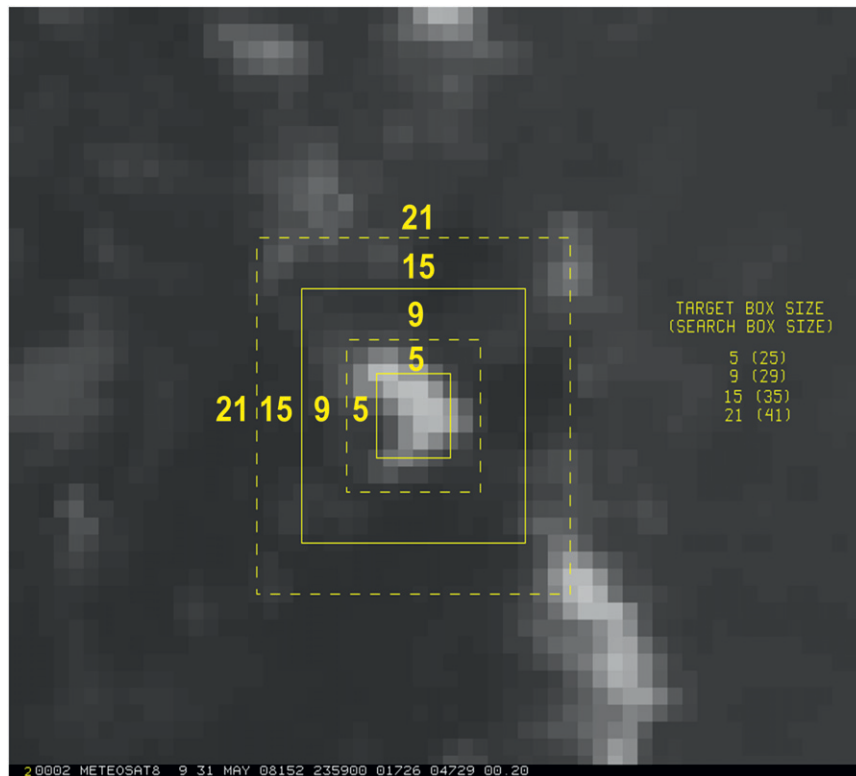


FIG. 3. The experimental setup, showing the various target box sizes tested and how each box was centered on the same initial location. The spacing between center points was equal to the largest box size tested (21 pixels).

2. Time-interval and tracking-window-size testing

Studies by SB and CHO show a direct link between the size of the target window and the magnitude of the AMV slow speed bias. These studies demonstrated that the size of the target window affects not only the speed of the derived estimate but also the height of the tracer. To be specific, the authors found that processing with a small target window yields lower height assignments and slightly faster derived-motion estimates. Because wind speeds generally increase with height in the troposphere, both factors combine to reduce the slow speed bias when compared with winds derived using a larger target window. Here we extend the results of SB and CHO by testing the effect of smaller target-window sizes, as well as varying time intervals, on the quality of the derived AMVs.

The image triplets used in our study were constructed from rapid-scan *Meteorological Satellite-8* (*Meteosat-8*) 10.8- μm imagery. A total of 16 different processing configurations were tested, including four target-window sizes (5×5 , 9×9 , 15×15 , and 21×21 pixels) and four image-loop time intervals (5, 10, 15, and 30 min). Figure 3 shows the experimental setup used during testing. Note

that the smallest target-window size tested, 5×5 pixels, is smaller than the one considered by SB (8×8 pixels). This was done deliberately to see whether the trends they observed extended to smaller box sizes. The configuration testing was performed with a version of the derived-motion-winds (DMW) algorithm (Daniels et al. 2010) developed for the future GOES-R Advanced Baseline Imager (ABI) that is closely based on the operational NOAA/NESDIS winds algorithm (Nieman et al. 1997; Velden et al. 2005), which finds a match of the initial target scene in a subsequent image by minimizing the SSD measure over a search region. The squared differences in the summation are computed using the brightness temperature values from the initial and search images. Image loops were created with the time intervals noted above by using three 10.8- μm images from *Meteosat-8* rapid scan data for the period 1–8 June 2008. The image triplets were centered at 0000 and 1200 UTC so that comparisons could be made with rawinsonde winds. Starting from the middle image, cloud features were tracked backward in time, to the first image in the loop, and then forward in time, to the third image in the loop. The resulting subvectors were averaged together to produce the final motion estimate. Tracking from the middle

image allowed us to use the same starting image and target locations in each of the tests, thus facilitating a direct one-to-one intercomparison of results. Quality statistics were compiled for each of the processing configurations by comparing the satellite-derived estimates with wind observations from the rawinsonde network following recommendations of the Coordination Group for Meteorological Satellites (CGMS) (e.g., Velden and Holmlund 1998). We note that the current testing was designed to mimic the procedure used by SB, who kept the target locations fixed while they expanded the window incrementally about the same central point. In effect, this produces a fixed “grid” of points, with the grid spacing equal to the size of the largest box size tested (21 pixels). This procedure of producing winds on a grid is a departure from the practice followed in NESDIS operations of centering the box on the maximum brightness gradient within the cloud scene but was necessary to keep the target locations the same in all tests. A short-range forecast from the National Centers for Environmental Prediction (NCEP) Global Forecast System (GFS) model was used to position the search box in the subsequent image while the following constraint was used to determine the size of the search box (for brevity, only the u -component equation is shown):

$$(u - u_g) \leq \frac{(L - 2)x}{2t}, \quad (1)$$

where L is referred to as the lag size and is the maximum displacement (in pixels) of a candidate match away from the center of the search box, t is the time interval in minutes, u is the AMV u -component (east–west) wind, u_g is the forecast (i.e., first guess) u -component wind, and x is the resolution in kilometers. Equation (1) is a constraint on the maximum departure permitted from the forecast by the bounds of the search region. If the constraint is held constant, then the size of the search box can be computed. Here we used a very loose constraint of 30 m s^{-1} to minimize the influence of the forecast on the results. If one substitutes 30 m s^{-1} into the left-hand side of Eq. (1), the equation for the lag size becomes

$$\frac{60}{x}t + 2 = L. \quad (2)$$

If the constraint in Eq. (1) is constant, then Eq. (2) implies that the lag size should be increased if the loop time interval is increased. Once the lag size is known, the search box size is computed from

$$S = T + L - 1, \quad (3)$$

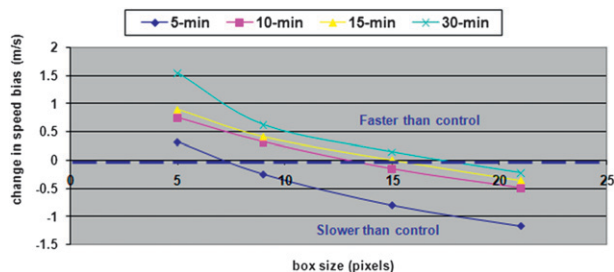


FIG. 4. Change in speed bias relative to control (box size of 15 pixels and time interval of 15 min) of various test configurations. Winds were derived from *Meteosat-8* IR imagery valid at 0000 and 1200 UTC for the period 1–8 Jun 2008.

where S is the search box size in pixels and T is the target box size in pixels. Given that the size of the search box is linked to the lag size by Eq. (3), it too should be expanded if the loop time interval is increased.

Throughout this paper the feature tracking was performed by minimizing the SSD between the target-scene brightness temperature field and the match-scene brightness temperature field. The SSD method is defined by

$$\sum_{x,y} [I_1(x,y) - I_2(x,y)]^2, \quad (4)$$

where I_1 is the brightness temperature at pixel (x, y) of the target scene and I_2 is the brightness temperature at pixel (x, y) of the search scene. The SSD method was chosen over a cross-correlation approach because it is computationally more efficient and produces superior results in regions of low contrast (Dew 2005).

Figure 4 shows the impact of the various processing configurations on the speed bias relative to a control run using an image time interval of 15 min and a target-window size of 15 pixels (the same settings used in NESDIS operations). It is clear from this figure that one way to minimize the slow speed bias is to shrink the size of the target window. Consistent with the findings of SB and CHO, the speed bias is reduced through a combination of faster motion and lower height assignments (not shown).

The lower height assignments associated with a small target window can be understood if one considers the manner in which most AMV data producers assign a height to an opaque cloud. It is common practice for producers to use a cold sample of points from the cloud scene instead of estimating the height from the entire sample of cloudy pixels (Merrill 1989; Nieman et al. 1997; Genkova et al. 2008). The operational NOAA/NESDIS winds algorithm, for example, uses the coldest 25% of pixels in the cloud scene to compute an average $11\text{-}\mu\text{m}$ brightness temperature. The location of this average temperature in a forecast temperature profile is assumed

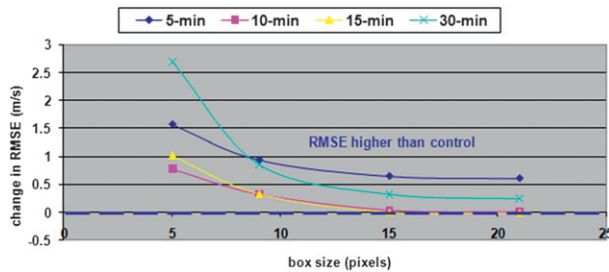


FIG. 5. As in Fig. 4, but for RMSE.

to be the height of the tracer. As a consequence, the height derived from a large target window tends to be higher than the height derived from a small target window.

The higher wind speeds associated with a smaller window are a little harder to explain, especially if one accepts the explanation given above for the differences in height assignment. One could argue that the colder sample from the larger window, being associated with higher cloud tops, should also be associated with faster wind speeds; SB concluded that the winds derived using a small target window more accurately reflect the motion on a local scale, whereas the winds derived using a large target window reflect the mean synoptic-scale motion over some depth of the atmosphere. In other words, a large target window is more likely to contain motions on varying spatial and temporal scales and possibly at different levels. As we show in the next section, the increased averaging of motions inherent with a large tracking window is an important contributor to the observed slow speed bias.

A less intuitive result of our testing is the observation that using a larger time interval can also minimize the speed bias. This behavior most likely reflects the ability of the large time intervals to better resolve slow wind speeds, meaning that slow-moving features are allowed to move farther as the time interval increases, which in turn minimizes the impact of subpixel displacement errors on the motion estimate. It appeared from our testing that the main impact of these subpixel errors was a slowing down of the derived-motion estimate at slower wind speeds. Histograms of wind speed (not shown) reveal that the peak frequency is shifted toward higher wind speeds as the image time interval increases.

It is tempting to suggest that a small target window be used to mitigate the slow speed bias problem. The use of a small target window increases the risk of finding a false match, however, which has the undesirable effect of adding noise (random error) to the retrieved winds. Figure 5 bears this fact out by showing a sharp increase in the RMSE value at the smallest target window size.

The preceding results imply that the problem of slow speed bias cannot be addressed simply by reducing the size of the target window. Any new approach that utilizes

a small window to minimize averaging must avoid introducing into the tracking solution random errors from finding false matches. In the next section we discuss a new approach that accomplishes this goal.

3. Nested tracking

We have developed a new nested-tracking approach that directly addresses two factors that are suspected to contribute to the slow speed bias associated with satellite-derived winds. The first is the excessive averaging, or smoothing, that can occur if multiple scales of motion are represented in the target window or if motion at two or more levels is detected. The second factor is an improper height assignment—one that is too high (from cold sampling) and may not be linked to the same pixels contributing to the motion estimate.

The nested-tracking approach utilizes a small tracking window to minimize averaging and produce faster wind estimates but does so without introducing the random tracking errors associated with a small window. Moreover, the approach is able to identify the pixels that have the greatest influence on the motion estimate. Using this information, together with the a priori knowledge of cloud height at each pixel, we are able to establish a direct link between the observed motion and the height of the tracer.

The new tracking approach involves deriving a motion estimate for all possible 5×5 pixel subregions “nested” within the larger target window. Small 5×5 subregions are better suited than larger target windows for tracking the small-scale motion that is representative of the instantaneous wind. The new approach produces a field of local motion vectors associated with each target window. Hereinafter, we use the term target window when referring to the outer box and subregion when referring to the smaller 5×5 box used to derive the local motion. A schematic of the nested tracking approach is shown in Fig. 6, followed by one example of its use in Fig. 7. Differences in orientation and magnitude can arise between the local motion vectors if more than one cloud layer is contained in the target window or if multiple scales of motion are detected. Outliers—those wind vectors that differ substantially from the majority of the sample—can result if the cloud is evolving or if the 5×5 subregion is too small to resolve the true motion. The latter is a manifestation of the so-called aperture effect, discussed at length in the field of computer vision (Trucco and Verri 1998). Note the close agreement between the average of the local motion vectors (green arrow) and the control vector (red arrow), derived by tracking the entire scene. The close agreement between the average local motion vector and the control vector is

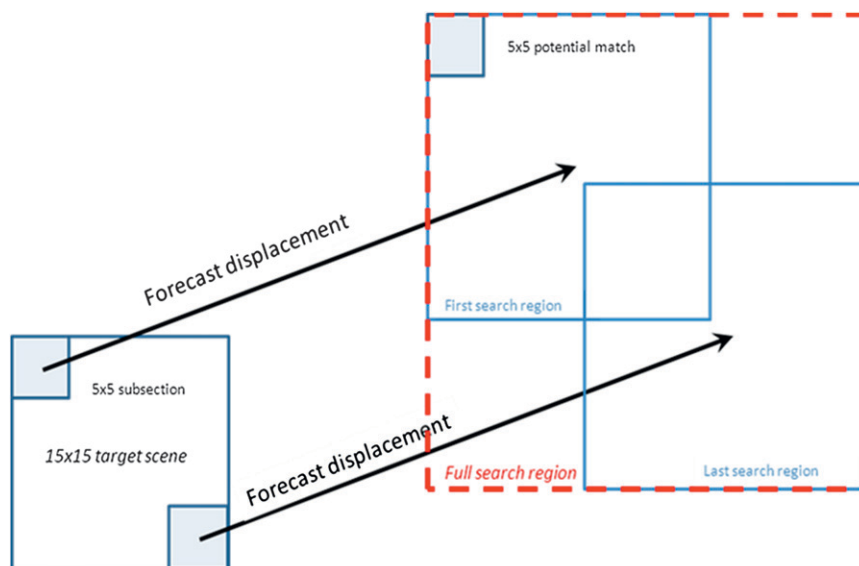


FIG. 6. Schematic that details the nested-tracking algorithm.

confirmation that the motion estimate derived using a traditional approach can be interpreted as an average of the instantaneous wind field. Furthermore, the bigger the tracking box is made, the greater is the implied averaging. Figure 7 also suggests an improved motion estimate might be derived if the noisy vectors could be removed and the dominant motion could be isolated. One way of accomplishing this is by using a cluster-analysis algorithm to analyze the displacements.

a. Identifying the dominant motion

The justification for using a cluster-analysis algorithm to analyze the local motion field is twofold. First, as

illustrated in Fig. 7, the local motion field can be very noisy. As discussed previously, this is due in part to the increased chance of finding a false match when using a small tracking box, as well as the cloud scene possibly containing motion associated with two or more cloud layers and/or motions that are representative of different spatial scales. Removing noise and separating the sample into coherent motion clusters can prevent the excessive averaging of these different motions and can reduce their contribution to a slow speed bias. Second, identifying clusters in the local motion field provides a means for directly linking the tracking and height assignment steps. In other words, using only the pixels

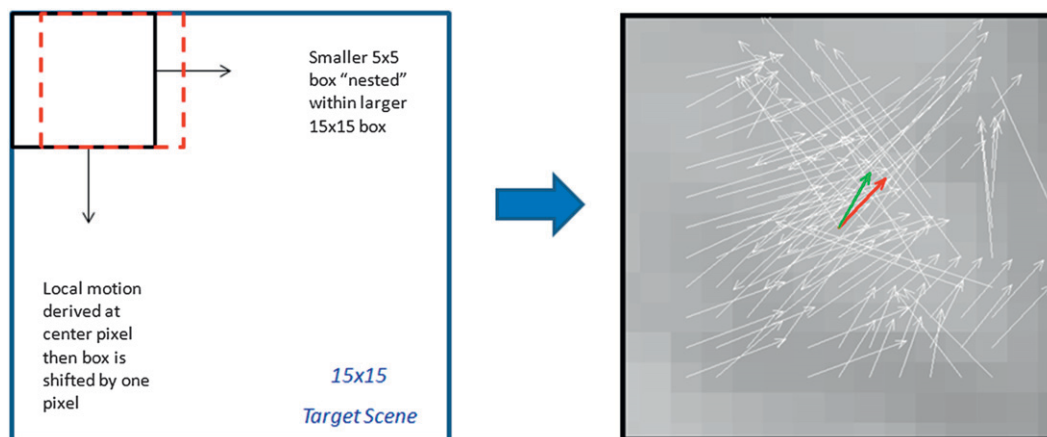


FIG. 7. An example of the local motion field derived with nested tracking. The white vectors show the local motion derived with a 5×5 box centered on the pixel location. The average local motion vector is shown in green, and the vector derived by tracking the entire scene is shown in red. Note that local motion vectors are not generated near the boundary where a full 5×5 box does not exist.

belonging to coherent motion clusters allows us to limit the sample of points used for height assignment to only those pixels that are important for tracking. This will be discussed later in the paper. First we discuss the problem of isolating the distinct motion clusters.

The cluster-analysis algorithm we selected is called density-based spatial clustering of applications with noise (DBSCAN; Ester et al. 1996). As its name implies, it is a density-based algorithm for identifying clusters in spatial databases with noise. It was chosen because it is very effective at identifying clusters of varying shapes and, unlike other methods such as k means, does not require the user to specify a priori the number of clusters to find. Instead, the user specifies two parameters; the minimum number of points defining a cluster, and the “neighborhood” size, which is used to discriminate between interior points (also called core points) and boundary points of a cluster. Ester et al. (1996) suggested using a minimum cluster size of four for 2D data, and this value was adopted in our study. The neighborhood size was determined empirically and is currently set at one-half of a pixel. Such a small neighborhood size is possible because the integer displacements produced by the tracking step are refined by linearly interpolating between the SSD values surrounding the minimum. As noted in the introduction, this is a common practice of operational wind producers that avoids “binning” the motion estimates by speed.

Before invoking the clustering algorithm, we compute a local motion estimate for all 5×5 subregions contained within the target window using the nested-tracking approach. As before, we start from the middle image and use the SSD method to find the scene that most closely resembles the initial subregion from a successive image. Only full 5×5 subregions are tracked, and each local motion vector is assigned to the location of the center pixel. In addition, to avoid gross mismatches, we limit the initial sample to those matches possessing a correlation score of 0.8 or higher. This produces a set of line (north/south) and element (east/west) displacements for the reverse vector and a separate set of displacements for the forward vector for each target window. Each set of displacements is then analyzed with DBSCAN to filter out noise and to find the coherent motion clusters. The line and element displacements of the *largest* (most populated) cluster are then averaged to obtain the dominant motion vector. The dominant motion vector for the reverse time step is averaged with the dominant motion vector of the forward time step to produce the final motion estimate. Note that, instead of averaging the two subvectors together, we could have combined the displacements from the reverse time step with the displacements from the forward time step and analyzed the

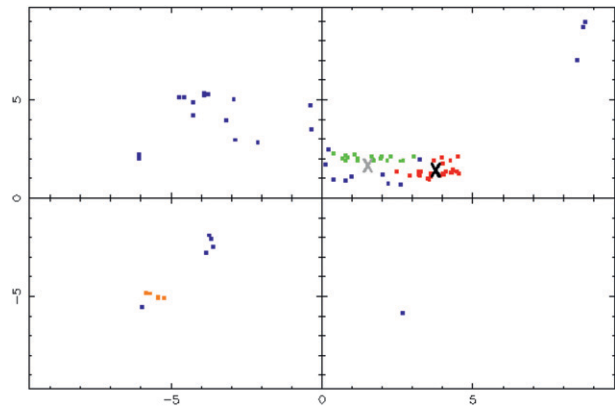


FIG. 8. DBSCAN output for the cloud scene pictured in Fig. 7. The two largest clusters are shown by the red and green dots. The average displacement of the points in the largest cluster is shown by the black “X” while the motion derived from tracking the entire scene is shown by the gray “X.” The other colors are explained in the text.

combined sample with DBSCAN. We chose not to take this approach, however, because we wanted to compute the acceleration between the reverse vector and the forward vector and to use it as a gross error check. Figure 8 shows the output obtained after applying DBSCAN to the set of local motion displacements shown in Fig. 7. In this case, the clustering algorithm finds two primary motion clusters, with the largest cluster shown in red and the second largest cluster shown in green. A third smaller cluster is shown in orange. The points that do not belong to any cluster (i.e., noise) are shown in blue. The black “X” shows the average displacement of points in the largest cluster. It is important to note that this displacement is very different from the displacement indicated by the gray “X,” which is the solution obtained by tracking the entire cloud scene.

b. Case-study examples

Here we present two examples highlighting the new nested-tracking approach. The first example, Fig. 9, is the accompanying vector plot for the DBSCAN example shown in Fig. 8. It highlights a fairly complex and evolving cloud scene at upper levels. Figure 9 graphically depicts the filtering performed by the clustering. This filtering can be thought of as a two-stage process. The first stage removes noise from the data, and the second stage isolates the largest cluster. It is clear that the cluster analysis has removed many of the vectors that “cancelled” one another in the initial sample. By doing so, the motion estimate has increased from 16.4 m s^{-1} (red vector) to 23.6 m s^{-1} (green vector).

A second example, shown in Fig. 10, is included to demonstrate an additional potential use of the new tracking approach—the ability to produce more than one useful

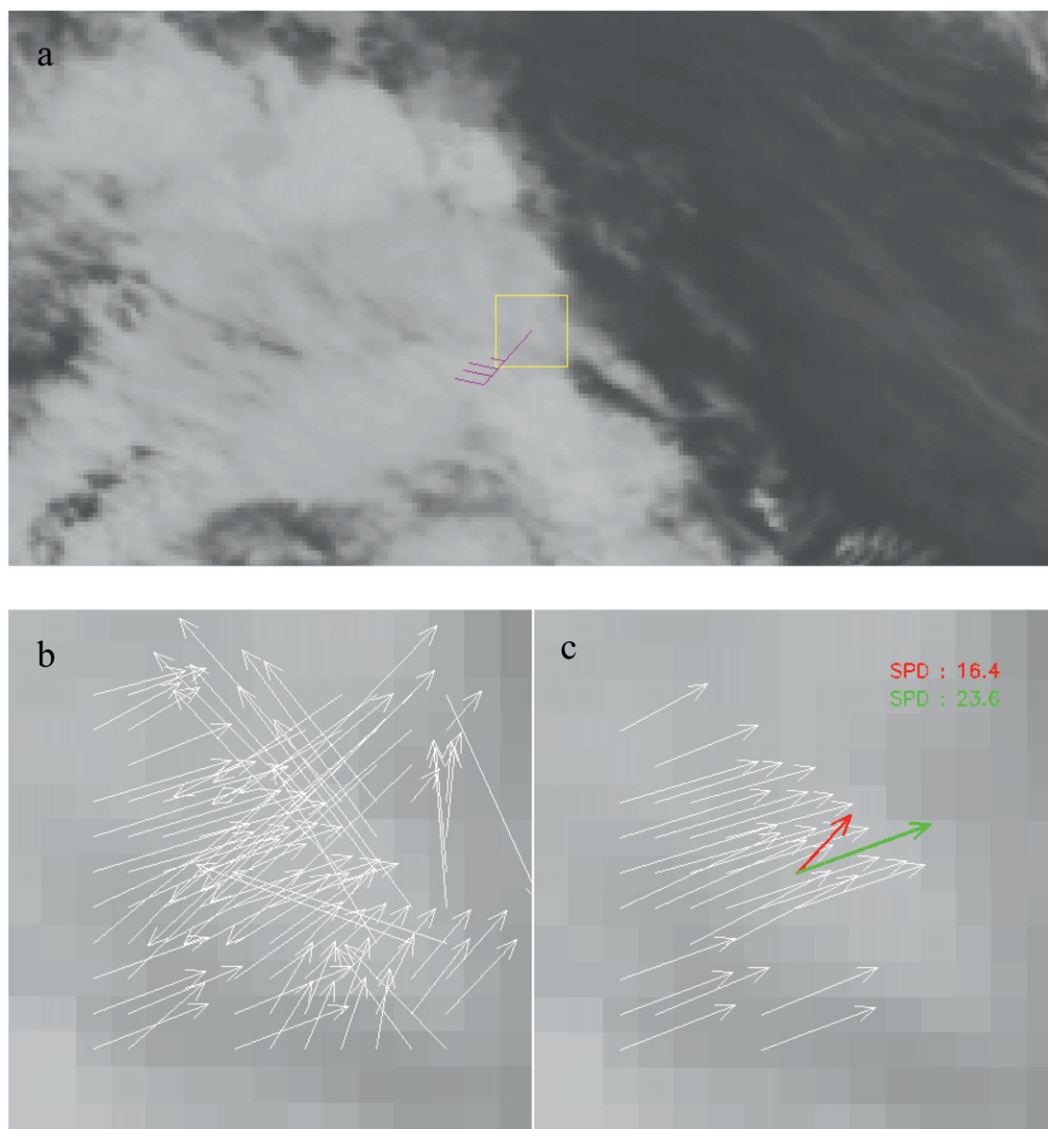


FIG. 9. Example of vector field produced with nested tracking (b) before and (c) after DBSCAN is applied to find the largest cluster. Plotted in green is the average displacement associated with the points in the largest cluster. Plotted in red is the motion derived by the operational tracking method. Speed units are meters per second. (a) A wider view of the scene, with the control vector plotted in magenta (kt ; $1 \text{ kt} \approx 0.5 \text{ m s}^{-1}$).

motion estimate from a single cloud scene. This figure shows a well-defined frontal zone associated with an extratropical low pressure system. The cluster analysis of this cloud scene reveals two primary motion clusters, one associated with the synoptic-scale motion of the frontal zone and the second showing motion within the frontal zone itself. In this particular case, it is the second motion estimate that stands as a much better match to a coincident rawinsonde observation (light blue vector in Fig. 10a).

The preceding examples help to illustrate an important detail—the points in the final sample do not always coincide with the location of the coldest cloud tops. This

is underscored by Fig. 11, which shows the cloud-top-pressure distribution for a single target scene. The black histogram shows the distribution of all cloudy pixels in the scene, whereas the green histogram shows the distribution associated with the largest motion cluster. Very few of the points in the largest motion cluster are located in the coldest portion of the histogram (to the left of the red line). Perhaps not surprising is that there is a tendency for the nested-tracking approach to retain vectors in regions of enhanced structure, where a second strong gradient in the brightness temperatures exists. These so-called corner points (a feature with two or

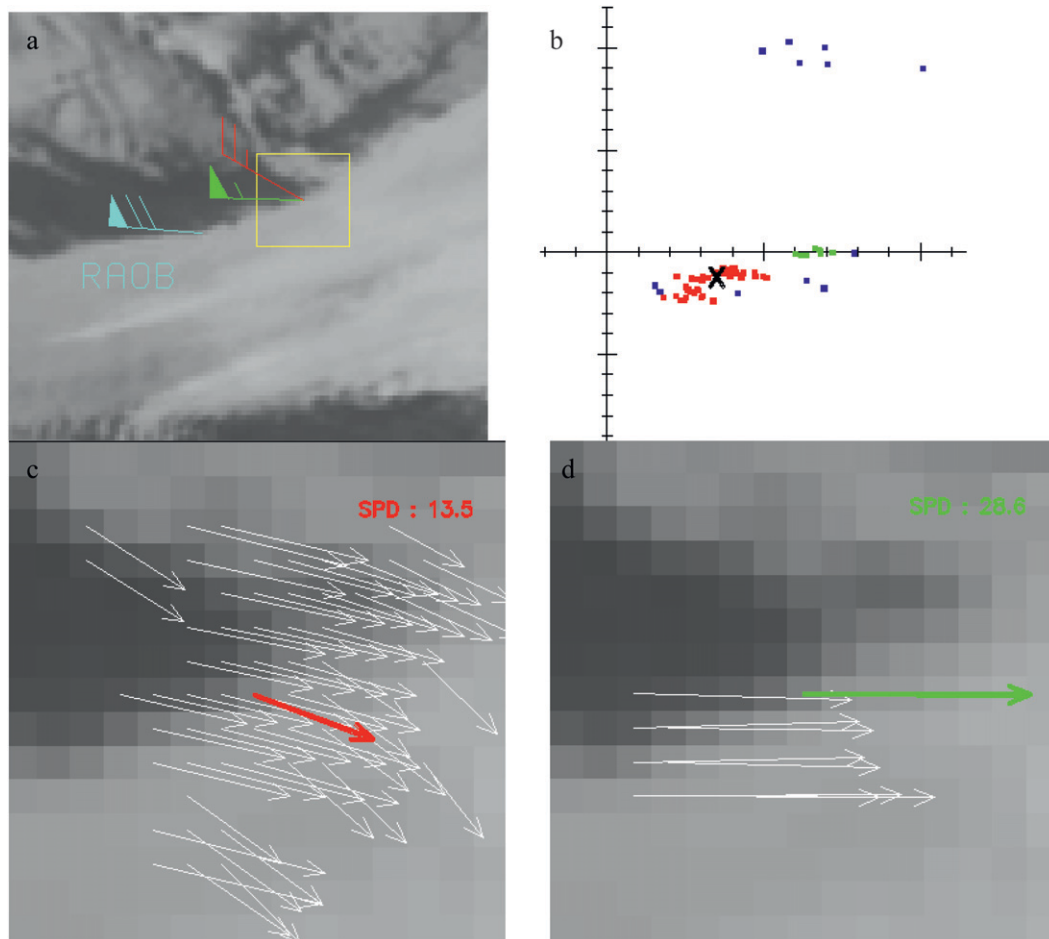


FIG. 10. DBSCAN analysis of local motion near a frontal zone: (a) *Meteosat-8* IR image at 1200 UTC 1 Feb 2007, (b) clusters found by DBSCAN, (c) local motion vectors associated with the largest cluster, and (d) local motion vectors associated with the second-largest cluster. In (a) the target box is outlined in yellow, the derived motion associated with the largest cluster is shown in red, and a nearby rawinsonde observation at 500 hPa is shown by the blue vector. In (b) the largest motion cluster is shown by the red points and the second-largest cluster is shown by the green points. The average displacement of the points in the largest cluster is shown by the "X." The colored vectors in (c) and (d) show the average motion of the cluster.

more well-defined edges) make for the most reliable tracers because they lessen the aperture effect mentioned previously (Trucco and Verri 1998). The most reliable 5×5 subtargets for tracking may unfortunately contain thin cloud layers or partly cloudy pixels, where cloud-top-height estimates are often less reliable. This issue needs to be kept in mind when assigning a representative height to the derived AMV. This issue is discussed further in the next section.

The fact that the points remaining in the final sample are not always the coldest pixels argues against using a cold sample of points to assign a height to the tracer. One logical alternative would be to assign a height on the basis of those points relevant to the tracking solution. This approach is discussed in the following section.

c. Linking height assignment with tracking

The GOES-R DMW algorithm runs within a processing framework that includes cloud algorithms developed by the GOES-R Algorithm Working Group (AWG) Cloud Team (Heidinger 2010; Heidinger et al. 2010; Pavolonis 2010). The cloud algorithms provide pixel-level output of cloud coverage, cloud phase, and cloud-top height.

As noted previously, a key benefit to using a cluster-analysis algorithm in tandem with nested tracking is that it allows us to identify those pixels contributing to the final motion estimate (i.e., the pixels in the largest motion cluster). By choosing the cloud-top-pressure value at the center of each 5×5 box as the pressure level of

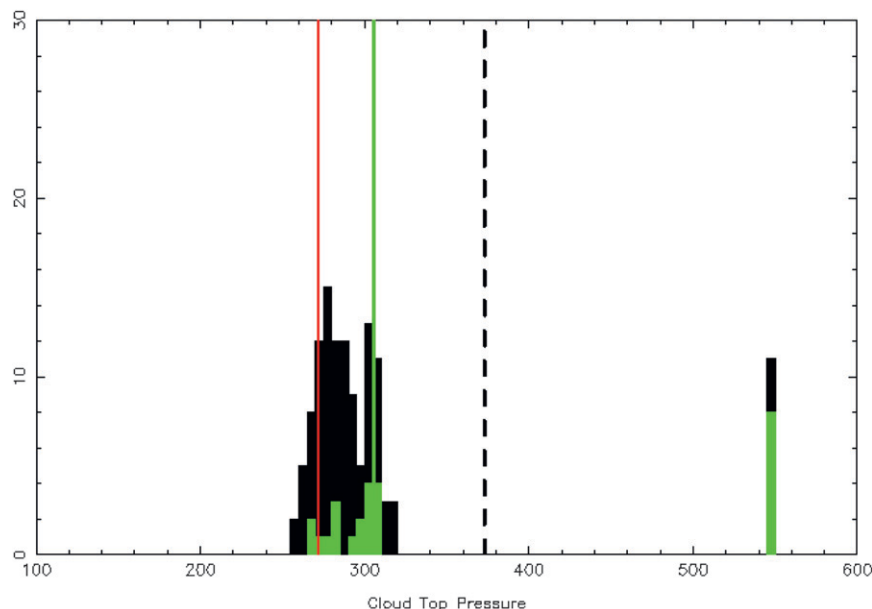


FIG. 11. Distribution of cloud-top pressure for a single target scene (15×15 pixels).

the local motion estimate we can construct a sample of cloud-top-pressure values associated with the largest motion cluster. The tracking process produces two such “intermediate” samples for each target scene; one sample is generated for the forward vector, and one sample is generated for the reverse vector. The median value of each sample serves as an intermediate pressure assignment for the AMV. A final pressure assignment is computed by combining the two intermediate samples and determining the median value of the combined sample. A similar procedure is followed to obtain the median cloud-top temperature and median cloud-top height of the AMV. The alternative height assignment approach just described usually yields a height estimate that is significantly *lower* in the atmosphere than a height estimate computed from a cold sample drawn from the entire target window. One example highlighting this fact is shown in Fig. 11. In Fig. 11 two peaks in the cloud-top-pressure distribution occur between 250 and 320 hPa, with a third peak located around 550 hPa. The median of the cold sample (red line) is approximately 35 hPa above the median of the largest motion cluster (green line). Also shown in in Fig. 11 is the mean pressure (black dashed line) of the largest motion cluster. Note that the median value is less influenced by the outliers at 550 hPa than is the mean. This is an important point and will be discussed further below. Figure 11 is consistent with the observation made earlier that the final sample of points in the largest motion cluster may not coincide with the coldest pixels. One concern we have with coupling the tracking and height-assignment

processes in this manner is that it might increase the reliance of the final height assignment on less-reliable cloud-top-height information near cloud edges. To address this concern, we limit the final sample of points in the largest motion cluster to those pixels deemed cloudy or probably cloudy by the cloud-mask algorithm. Furthermore, we compute a median value of the cloud-top-pressure distribution instead of computing the mean value, which is less robust to outliers (Press et al. 1986). Figure 11 highlights the robustness of the median, relative to the mean, in the presence of outliers. We have also implemented a maximum-difference (100 hPa) threshold on the median values associated with each subvector and discard any AMVs that exceed this threshold. Last, we are in the process of testing a 3D DBSCAN analysis that includes the height dimension to limit the variability in the cloud-top pressure estimates.

4. Impact of nested tracking on AMV quality

To assess the accuracy of AMVs derived with the new approaches, image triplets, composed of *Meteosat-8* 10.8- μm imagery centered at 0000 and 1200 UTC, were processed for August of 2006 and February of 2007 and the derived winds were compared with coincident rawinsonde observations. Winds were generated over the entire full disk domain using successive images separated by a 15-min time interval. In addition to the test winds, two control sets of AMVs were generated using the conventional tracking and height-assignment approaches employed by the operational NOAA/NESDIS

TABLE 1. AMV–rawinsonde collocation statistics (m s^{-1}) for February 2007.

	Control 19×19 box	Nested tracking
All levels (100–1000 hPa)		
RMSE	7.43	6.81
Speed bias	−2.47	−0.12
Avg AMV speed	16.37	16.69
Avg pressure (hPa)	442	509
Sample	13 105	13 105
High level (100–400 hPa)		
RMSE	8.42	7.82
Speed bias	−3.00	−0.10
Avg AMV speed	19.58	20.06
Avg pressure (hPa)	281	335
Sample	7317	7317
Midlevel (400–700 hPa)		
RMSE	6.98	6.10
Speed bias	−2.36	−0.08
Avg AMV speed	13.98	14.16
Avg pressure (hPa)	526	621
Sample	3356	3356
Low level (700–1000 hPa)		
RMSE	4.08	3.88
Speed bias	−0.99	−0.25
Avg AMV speed	9.99	10.06
Avg pressure (hPa)	812	879
Sample	2433	2433

TABLE 2. As in Table 1, but the comparison is with a control run using a 5×5 box.

	Control 5×5 box	Nested tracking
All levels (100–1000 hPa)		
RMSE	6.96	6.54
Speed bias	−1.15	0.61
Avg AMV speed	18.42	18.11
Avg pressure (hPa)	410	476
Sample	1208	1208
High level (100–400 hPa)		
RMSE	7.52	7.25
Speed bias	−1.44	0.60
Avg AMV speed	21.03	20.75
Avg pressure (hPa)	275	328
Sample	768	768
Midlevel (400–700 hPa)		
RMSE	7.11	6.05
Speed bias	−0.96	1.12
Avg AMV speed	16.67	16.23
Avg pressure (hPa)	496	605
Sample	231	231
Low level (700–1000 hPa)		
RMSE	3.96	3.75
Speed bias	−0.29	0.11
Avg AMV speed	10.77	10.47
Avg pressure (hPa)	807	881
Sample	209	209

algorithm. One control set was generated by using a 19×19 target box, and the second control set was generated by using a 5×5 target box. Both control runs utilized a cold sample (coldest 25%) of points from the target box to assign a height to the AMV. The assigned height in each case was the median cloud-top pressure of the cold sample distribution. The first control configuration mirrors the traditional approach followed by AMV producers to generate derived-motion winds, and the second control configuration was added to measure the impact of the new approaches (DBSCAN filtering and height reassignment) on AMV quality. The second control configuration is an attempt to separate the impact of a reduction in target-box size from the impact of the DBSCAN filtering and height reassignment steps.

Table 1 shows the AMV–rawinsonde collocation statistics for February of 2007 for the 19×19 control winds and the new nested-tracking winds sorted by pressure layer (all levels, high, middle, and low), as is the standard CGMS convention for reporting AMV verification statistics. One immediately notices the much-improved value for the speed bias in the test output. The improvement in the speed bias is achieved through a combination of lower height assignments (note the nearly 70-hPa difference in average pressure between the control and the test) and faster wind speeds. Although greatest at upper

levels, the improvement in the speed bias is evident throughout the atmosphere. This intuitively makes sense because the risk of capturing motion at multiple levels is greatest at upper levels. Note also in Table 1 that the RMSE is much improved in the test case and that a similar tendency exists for the improvement to increase with height.

Table 2 shows the AMV–rawinsonde collocation statistics for February of 2007 for the 5×5 control and test winds. As noted above, this comparison was performed with the aim of separating the impact of a reduction in target-box size from the impact of the DBSCAN filtering and height-reassignment steps. The sample size for this comparison is unfortunately much smaller, which is an indication that most target locations were different in the two samples. A collocation was not performed unless the center of the 5×5 box coincided exactly with the center of the nested-tracking target box. Still, the conclusions drawn from the second comparison are very similar to the conclusions from the first comparison. The speed bias is again much improved in the test relative to the control, but the disparity between the test value and the control value is less dramatic (note the smaller change in the speed bias between the test and control in Table 2). One reason the impact is smaller is that the average speed of the control (18.42 m s^{-1}) is now greater than the

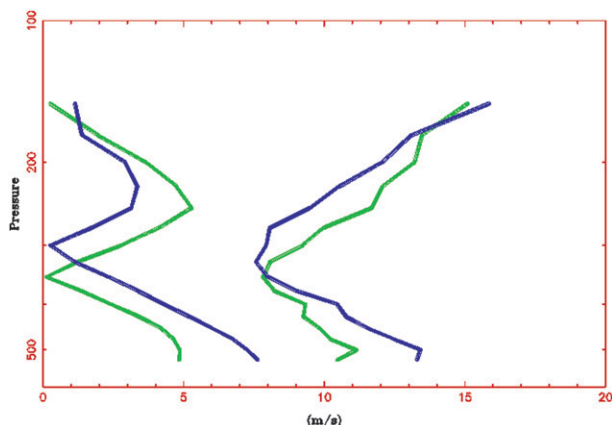


FIG. 12. Profiles of RMSE (profiles on right) and absolute speed bias (profiles on left) at 300 hPa for August 2006 and February 2007 for the control (green) and test (blue).

average speed of the test (18.11 m s^{-1}). This is to be expected given that the derived speed in the control reflects the motion of a single 5×5 box, whereas the derived speed in the test is an average motion of many 5×5 boxes. One unexpected result of the second comparison is a fast bias for the nested-tracking winds. The fast bias suggests that the AMV height assignments might be too low, especially in the middle of the atmosphere. A more definitive conclusion is not possible, however, because of the small sample size.

Figure 12 shows the average AMV-rawinsonde RMSE and absolute speed bias profiles for the 300-hPa level for August of 2006 and February of 2007. In the ideal

case, the level of best fit (minimum in RMSE or speed bias) would coincide with the assigned pressure level (300 hPa). One measure of the goodness of the fit is the vertical departure of the minima from the assigned AMV pressure level. For the control, the disparity between the assigned AMV level and the level of best fit is roughly 50 hPa. For the test, the disparity is 25 hPa for the RMSE profile and 0 hPa for the absolute speed bias profile. The profiles suggest that the cold sample heights are too high in the atmosphere and that the new heights (and winds) are a better fit to the rawinsonde observations. A histogram of speed bias values for August of 2006 (Fig. 13) confirms this result.

5. Summary and future plans

A nested-tracking algorithm has been developed to minimize the slow speed bias commonly observed with satellite-derived AMVs at mid- and upper levels of the atmosphere. By using small subregions (5×5 pixel box) nested within a conventional target window, the algorithm produces a set of local motion vectors for each cloud scene. The field of local motion vectors is subsequently analyzed with a cluster-analysis algorithm to remove outlying motions and to isolate distinct motion clusters that can represent motion at different scales or heights. Clustering of the computed displacements has the major advantage of minimizing the averaging of motions at different scales or different levels that can occur if too large a target window is used for tracking. In general, nested tracking yields slightly faster derived

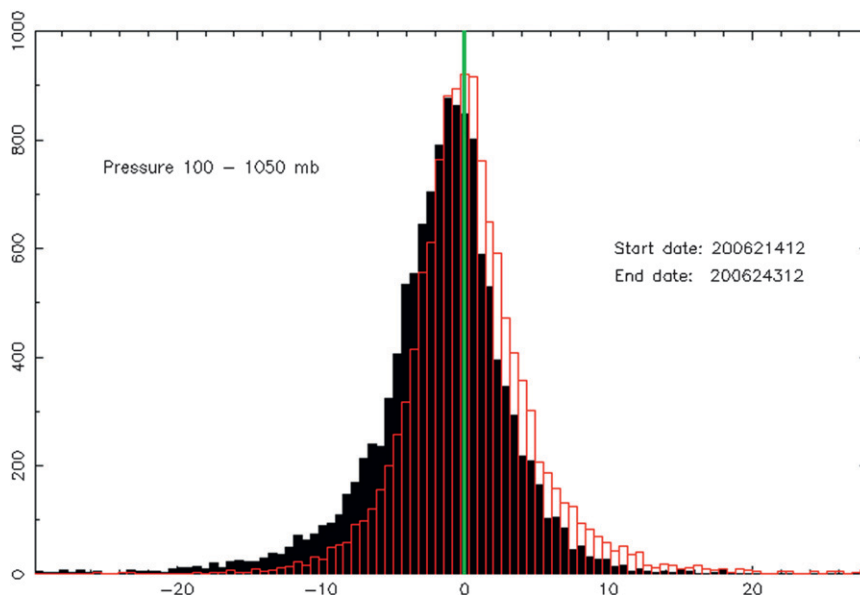


FIG. 13. Histogram of speed bias values for August 2006 for the control (solid black) and test (red).

motions than does a more conventional tracking approach. For multilayer cloud scenes or situations in which the clouds are evolving, however, the speed adjustment can be much larger.

Another advantage of the nested-tracking approach is its ability to identify which pixels within the cloud scene are contributing to the tracking solution. Knowing which pixels are contributing to the dominant motion allows for a more representative height to be computed and assigned to the AMV. This, in turn, directly links the height-assignment and tracking processes. In general, the new height-sampling approach yields considerably lower (by roughly 70 hPa) height estimates than do those based on a cold sample of pixels.

Comparison statistics between AMVs derived using *Meteosat-8* IR imagery and collocated rawinsondes for August of 2006 and February of 2007 show that the new methods substantially reduce the slow speed bias. The reduction in bias is accomplished through a combination of faster winds and lower height assignments. Furthermore, the AMVs derived with the new approaches show a significant improvement in quality (as indicated by the RMSE) versus AMVs derived with more conventional methods.

The new methods discussed in this paper represent core components of the derived-motion-winds algorithm developed for the future GOES-R ABI. We have initiated work (Nebuda et al. 2011) to perform numerical weather prediction model impact studies using NCEP's Global Forecast System to assess the impact of winds derived from the nested-tracking approach on the accuracy of GFS model forecasts. Given the significant improvement in quality we have observed with these new approaches, we are hopeful that they will have a positive impact on the accuracy of GFS forecasts. If successfully demonstrated, our plans call for this new winds algorithm to replace the current operational derived-motion-winds algorithm running at NOAA/NESDIS. In addition, as part of this effort we plan to take a look at the wind information content contained in the second- and third-largest clusters to see if there are situations in which this information would be more useful than the wind information content derived from the largest cluster.

Acknowledgments. The authors thank Andrew Heidinger and the GOES-R AWG Cloud Team for providing the algorithms to generate the estimates of pixel-level cloud-top height.

REFERENCES

- Borde, R., and R. Oyama, 2008: A direct link between feature tracking and height assignment of operational atmospheric motion vectors. *Proc. Ninth Int. Winds Workshop*, Annapolis, MD, EUMETSAT, 8 pp. [Available online at http://www.eumetsat.int/Home/Main/AboutEUMETSAT/Publications/ConferenceandWorkshopProceedings/2008/groups/cps/documents/document/pdf_conf_p51_s3_13_borde_v.pdf.]
- Bormann, N., G. Kelly, and J.-N. Thépaut, 2002: Characterising and correcting speed biases in atmospheric motion vectors within the ECMWF system. *Proc. Sixth Int. Winds Workshop*, Madison, WI, EUMETSAT, 113–120. [Available online at http://cimss.ssec.wisc.edu/iwgg/iww6/session3/bormann_1_bias.pdf.]
- Cho, H.-J., E.-H. Sohn, and M.-L. Ou, 2008: The impact of target box size on wind speed biases in satellite-derived atmospheric motion vectors. *Proc. 2008 EUMETSAT Meteor. Satellite Conf.*, Darmstadt, Germany, EUMETSAT, 5 pp. [Available online at http://www.eumetsat.int/Home/Main/AboutEUMETSAT/Publications/ConferenceandWorkshopProceedings/2008/SP_1232700911980?l=en.]
- Daniels, J., W. Bresky, S. Wanzong, C. Velden, and H. Berger, 2010: GOES-R Advanced Baseline Imager (ABI) algorithm theoretical basis document for derived motion winds. GOES-R Program Office, 96 pp. [Available online at http://www.goes-r.gov/products/ATBDs/baseline/Winds_DMW_v2.0_no_color.pdf.]
- Dew, G., 2005: Investigation of target tracking techniques in the MSG MPEF environment. *Proc. Seventh Int. Winds Workshop*, Helsinki, Finland, EUMETSAT, 171–179.
- Ester, M., H.-P. Kriegel, J. Sander, and X. Xu, 1996: A density-based algorithm for discovering clusters in large spatial databases with noise. *Proc. Second Int. Conf. on Knowledge Discovery and Data Mining (KDD-96)*, Portland, OR, Association for Computing Machinery, 226–231.
- Forsythe, M., and R. Saunders, 2008: Third analysis of the data displayed on the NWP SAF AMV monitoring website. NWP SAF Tech. Rep. 22, 50 pp.
- Genkova, I., R. Borde, J. Schmetz, K. Holmlund, J. Daniels, and C. Velden, 2008: Global atmospheric motion vector inter-comparison study. *Proc. Ninth Int. Winds Workshop*, Annapolis, MD, EUMETSAT, 9 pp. [Available online at http://www.eumetsat.int/Home/Main/AboutEUMETSAT/Publications/ConferenceandWorkshopProceedings/2008/groups/cps/documents/document/pdf_conf_p51_s4_20_genkova_v.pdf.]
- Hayden, C. M., and S. J. Nieman, 1996: A primer for tuning the automated quality control system and for verifying satellite-measured drift winds. NOAA Tech. Memo. NESDIS 43, 27 pp.
- Heidinger, A., 2010: GOES-R Advanced Baseline Imager (ABI) algorithm theoretical basis document for cloud height. GOES-R Program Office, 77 pp. [Available online at http://www.goes-r.gov/products/ATBDs/baseline/Cloud_CldHeight_v2.0_no_color.pdf.]
- , M. J. Pavolonis, R. E. Holz, B. A. Baum, and S. Berthier, 2010: Using *CALIPSO* to explore the sensitivity to cirrus height in the infrared observations from NPOESS/VIIRS and GOES-R/ABI. *J. Geophys. Res.*, **115**, D00H20, doi:10.1029/2009JD012152.
- Merrill, R. T., 1989: Advances in the automated production of wind estimates from geostationary satellite imagery. Preprints, *Fourth Conf. on Satellite Meteorology and Oceanography*, San Diego, CA, Amer. Meteor. Soc., 246–249.
- Nebuda, S., J. Jung, D. Santek, J. Daniels, and W. Bresky, 2011: Evaluation and quality control of nested tracking approach for AMVs. *Proc. 11th Int. Winds Workshop*, Auckland, New Zealand, EUMETSAT, 17 pp. [Available online at http://cimss.ssec.wisc.edu/iwgg/iww11/talks/Session4_Nebuda.pdf.]

- Nieman, S. J., W. P. Menzel, C. M. Hayden, D. Gray, S. T. Wanzong, C. S. Velden, and J. Daniels, 1997: Fully automated cloud-drift winds in NESDIS operations. *Bull. Amer. Meteor. Soc.*, **78**, 1121–1133.
- Pavolonis, M., 2010: GOES-R Advanced Baseline Imager (ABI) algorithm theoretical basis document for cloud type and cloud phase. GOES-R Program Office, 96 pp. [Available online at http://www.goes-r.gov/products/ATBDs/option2/Cloud_CldType_v2.0.pdf.]
- Press, W. H., S. A. Teukolsky, W. T. Vetterling, and B. P. Flannery, 1986: *Numerical Recipes: The Art of Scientific Computing*. Cambridge University Press, 818 pp.
- Rohn, M., G. Kelly, and R. W. Saunders, 2001: Impact of a new cloud motion wind product from Meteosat on NWP analyses and forecasts. *Mon. Wea. Rev.*, **129**, 2392–2403.
- Schmetz, J., K. Holmlund, J. Hoffman, B. Strauss, B. Mason, V. Gaertner, A. Koch, and L. Van De Berg, 1993: Operational cloud-motion winds from Meteosat infrared images. *J. Appl. Meteor.*, **32**, 1206–1225.
- Sohn, E., and R. Borde, 2008: The impact of window size on AMV. *Proc. Ninth Int. Winds Workshop*, Annapolis, MD, EUMETSAT, 6 pp. [Available online at http://www.eumetsat.int/Home/Main/AboutEUMETSAT/Publications/ConferenceandWorkshopProceedings/2008/groups/cps/documents/document/pdf_conf_p51_s4_18_sohn_v.pdf.]
- Trucco, E., and A. Verri, 1998: *Introductory Techniques for 3-D Computer Vision*. Prentice Hall, 343 pp.
- Velden, C. S., and K. Holmlund, 1998: Report from the working group on verification and quality indices (WG III). *Proc. Fourth Int. Winds Workshop*, Saanenmoser, Switzerland, EUMETSAT, 19–20.
- , and K. M. Bedka, 2009: Identifying the uncertainty in determining satellite-derived atmospheric motion vector height attribution. *J. Appl. Meteor.*, **48**, 450–463.
- , and Coauthors, 2005: Recent innovations in deriving tropospheric winds from meteorological satellites. *Bull. Amer. Meteor. Soc.*, **86**, 205–223.
- , T. L. Olander, and S. Wanzong, 1998: The impact of multi-spectral *GOES-8* wind information on Atlantic tropical cyclone track forecasts in 1995. Part I: Dataset methodology, description, and case analysis. *Mon. Wea. Rev.*, **126**, 1202–1218.
- Von Bremen, L., N. Bormann, S. Wanzong, M. Hortal, D. Salmond, J.-N. Thepaut, and P. Bauer, 2008: Evaluation of AMVs derived from ECMWF model simulations. *Proc. Ninth Int. Winds Workshop*, Annapolis, MD, EUMETSAT, 8 pp. [Available online at http://www.eumetsat.int/Home/Main/AboutEUMETSAT/Publications/ConferenceandWorkshopProceedings/2008/groups/cps/documents/document/pdf_conf_p51_s5_26_bauer_v.pdf.]